DNA brick crystals with prescribed depths

Yonggang Ke[1,2,3]★†‡, Luvena L. Ong[1,4]‡, Wei Sun[1,5]‡, Jie Song[6], Mingdong Dong[6], William M. Shih[1,2,3] and Peng Yin[1,5]★

The ability to assemble functional materials with precise spatial arrangements is important for applications ranging from protein crystallography to photovoltaics. Here, we describe a general framework for constructing two-dimensional crystals with prescribed depths and sophisticated three-dimensional features. The crystals are self-assembled from single-stranded DNA components called DNA bricks. We demonstrate the experimental construction of DNA brick crystals that can grow to micrometre size in their lateral dimensions with precisely controlled depths up to 80 nm. They can be designed to pack DNA helices at angles parallel or perpendicular to the plane of the crystal and to display user-specified sophisticated three-dimensional nanoscale features, such as continuous or discontinuous cavities and channels.

The production of two-dimensional materials, particularly crystals with prescribed depths and intricate three-dimensional features, provides an enabling platform for nanofabrication. For example, these two-dimensional crystals could be integrated with inorganic nanomaterials to develop complex nanoelectronics[1] and photonics systems[2,3]. Although thin film structures have been created using either electron/ion beam lithography[3] or self-assembly of block copolymers[4,5], fabricating two-dimensional materials that simultaneously achieve precisely tunable thickness as well as prescribed complex surface and internal features (for example, channels or pores) with sub-5 nm resolution remains challenging[3,6–8].

A promising route to address this challenge is structural DNA nanotechnology[9]. DNA has been used to create complex discrete shapes[9–25] and extended periodic crystals[26–38], including ribbons[33], tubes[27,32,33,35], two-dimensional crystals[18,26–32,36–38] and three-dimensional crystals[34]. DNA structures can serve as scaffolds for precise patterning of functional moieties (for example, gold nanoparticles) for electronics and photonics applications[35,39,40]. However, in contrast to current organic polymeric films[41], the two-dimensional DNA crystals are typically restricted to a single layer of DNA helices with ∼2 nm depth. A three-dimensional crystal has been reported previously, but it grows in all three dimensions with no control in depth and uses a small triangular repeating unit[34]. One major categorical gap in constructing atomically precise DNA structures—and, more generally, synthetic molecular structures—is the lack of a general framework for making complex two-dimensional crystals with precisely controlled depths and sophisticated three-dimensional features. Successful construction of such structures could enable a wide range of applications ranging from nanoelectronics and plasmonics to biophysics and molecular diagnosis.

Using single-stranded DNA bricks[21,22,33], we describe here a simple, robust and general approach to engineer complex micrometre-sized two-dimensional crystals with prescribed depths and complex three-dimensional features with nanometre resolution. In previous reports[26–32,34–38], DNA crystals have typically been formed via a two-stage hierarchical process, in which individual strands first assemble into a discrete building block (often known as a DNA tile), and individual tiles then assemble into crystals. In contrast, DNA brick crystals grow non-hierarchically, and the growth of DNA crystals from short, floppy, single-stranded DNA bricks does not involve the assembly of preformed discrete multi-stranded building blocks with well-defined shapes. During the brick crystal growth, assembly and disassembly occur via relatively weak intermolecular interactions involving the addition or subtraction of a single short strand at a time.

We constructed a total of 32 DNA brick crystals. These crystals can grow up to several micrometres in their lateral dimensions with a prescribed depth of up to 80 nm, and display sophisticated user-specified nanometre-scale three-dimensional features, including intricate cavities, channels and tunnels (Supplementary Fig. 1). Additionally, the non-hierarchical nature of the assembly permits isothermal formation of the crystals. We illustrated the scaffolding utility of these crystals by functionalizing them with parallel arrays and layers of tightly packed (1–2 nm spaced) gold nanoparticles.

Design and assembly of DNA brick crystals

The crystal design was based on previous discrete three-dimensional DNA brick structures[22]. A DNA brick is a 32-nucleotide (nt) strand with four 8-nt binding domains, and can be modelled as a Lego-like brick (Fig. 1a). In a one-step annealing reaction, DNA bricks—each with a distinct sequence—assemble into a prescribed structure by binding to their designated neighbours. Implementing 'connecting' bricks between discrete structures yields DNA brick crystals. The design strategy is illustrated using a 6H (helix) × 6H (helix) × 24B (base pair) cuboid structure that can be programmed to grow along three orthogonal axes (Fig. 1b). To achieve growth along the z axis (parallel to the helical axes), the domains in the first layer are modified to be complementary to the domains in the last layer. Growth along the x axis or y axis is achieved by including bricks that each have two domains bound to one face of the cuboid and the other two domains bound to the opposing face (see Supplementary Fig. 2 for detailed strand connection patterns). The crystals are designed to form via non-hierarchical growth, with

[1]Wyss Institute for Biologically Inspired Engineering, Harvard University, Boston, Massachusetts 02115, USA, [2]Department of Cancer Biology, Dana-Farber Cancer Institute, Harvard Medical School, Boston, Massachusetts 02115, USA, [3]Department of Biological Chemistry and Molecular Pharmacology, Harvard Medical School, Boston, Massachusetts 02115, USA, [4]Harvard–MIT Division of Health Sciences and Technology, Massachusetts Institute of Technology, Cambridge, Massachusetts 02139, USA, [5]Department of Systems Biology, Harvard Medical School, Boston, Massachusetts 02115, USA, [6]Center for DNA Nanotechnology at the Interdisciplinary Nanoscience Center (iNANO), Aarhus University, 8000 Aarhus C, Denmark; †Present address: Wallace H. Coulter Department of Biomedical Engineering, Georgia Institute of Technology and Emory University, Atlanta, Georgia 30322, USA; ‡These authors contributed equally to this work. *e-mail: py@hms.harvard.edu; yonggang.ke@emory.edu
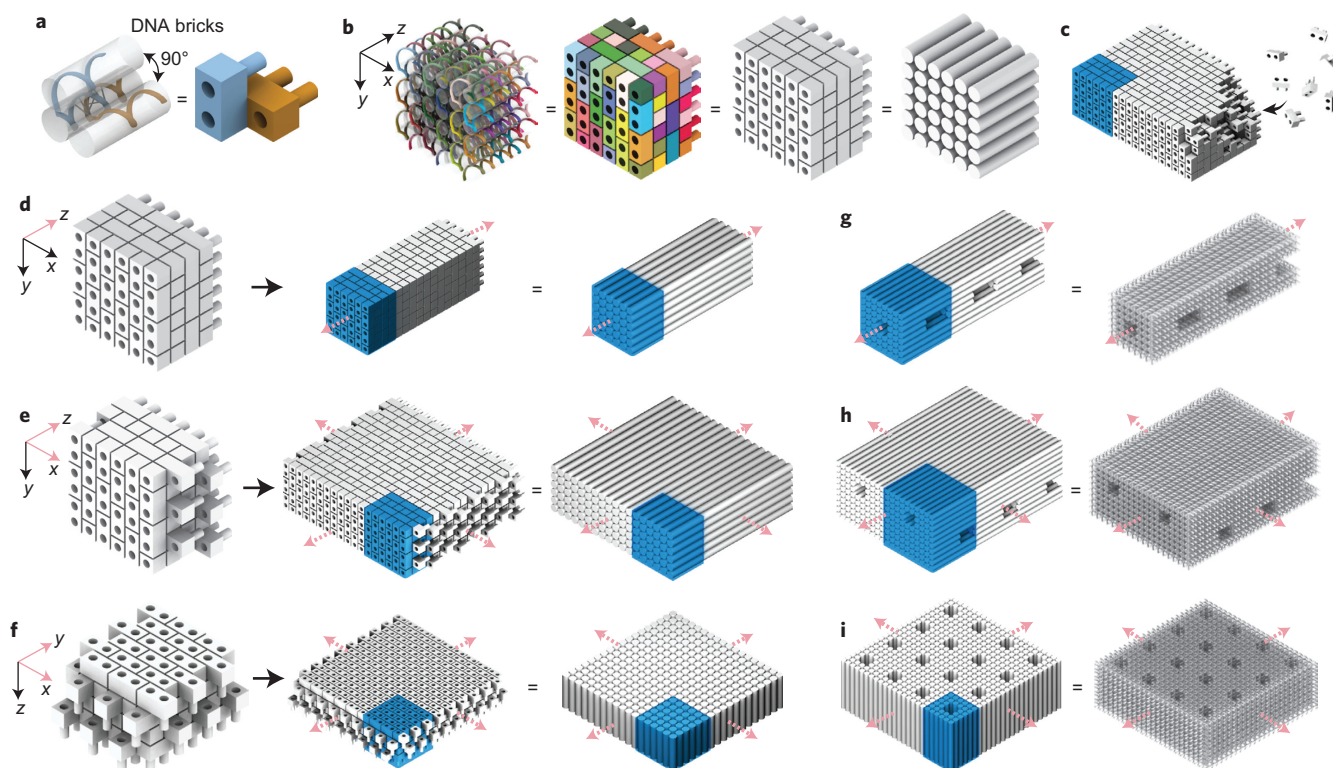
Figure 1 | Design of DNA brick crystals. a, Strand (left) and brick (right) models showing two 32-nt DNA bricks that form a 90° angle. **b**, Models of a 6H (helix) × 6H (helix) × 24B (base pair) cuboid with increasing levels of abstraction: (left to right) a strand model, a brick model (in which colours distinguish brick species), a brick model with all bricks coloured grey, and a model where cylinders represent DNA double helices. **c**, Individual DNA strands, rather than pre-assembled multi-brick blocks, are directly incorporated into the growing crystal. **d–f**, Brick and cylinder models of a one-dimensional Z-crystal (**d**), a two-dimensional ZX-crystal (**e**) and a two-dimensional XY-crystal (**f**) designed from the 6H × 6H × 24B cuboid. **g–i**, Cylinder and DNA-helix models of crystals with pores and tunnels: Z-crystal with a tunnel and periodic pores (**g**); ZX-crystal with two groups of parallel tunnels (**h**); XY-crystal with periodic pores (**i**). Repeating units of the crystals are denoted by blue boxes. Pink arrows indicate the directions of crystal growth.

individual bricks (rather than preformed multi-brick blocks) directly incorporated into the crystal (Fig. 1c).

We constructed four groups of crystals: (1) Z-crystals: one-dimensional 'DNA-bundle' crystals extending along the z axis (Fig. 1d); (2) X-crystals: one-dimensional crystals extending along the x axis; (3) ZX-crystals: two-dimensional 'multilayer' crystals extending along the z axis and the x axis (Fig. 1e); (4) XY-crystals: two-dimensional 'DNA-forest' crystals extending along the x axis and y axis (Fig. 1f). Using different designs of repeating units, DNA crystals with prescribed depths and features (for example, pores, channels and tunnels) can be made (Fig. 1g–i). Here, we define a 'channel' as a surface-exposed cavity extending across multiple repeating units, a 'pore' as a hole across a single repeating unit, and a 'tunnel' as a series of concatenated pores. A crystal is named as '[the growth direction(s)]–[the dimensions of the repeating unit]–[the shape of the unit]'. For instance, an 'XY-6H × 6H × 24B-cuboid' crystal is a two-dimensional XY-crystal with a cuboid-shaped 6H × 6H × 24B repeating unit. Like discrete DNA brick structures[22], the sequences for DNA-brick crystals were randomly generated. All crystals used a 10.67 base pair (bp)/turn reciprocal twist density, which is slightly underwound compared to the 10.5 bp/turn of natural B-form DNA.

Each crystal was assembled by mixing unpurified DNA brick strands in a roughly equimolar ratio in the presence of 40 mM $MgCl_2$, without careful adjustment of strand stoichiometry. After 72 h or 168 h one-pot annealing, assembled crystals were imaged using transmission electron microscopy (TEM), cryo-electron microscopy (cryo-EM) or atomic force microscopy (AFM), without further purification. See Methods for details.
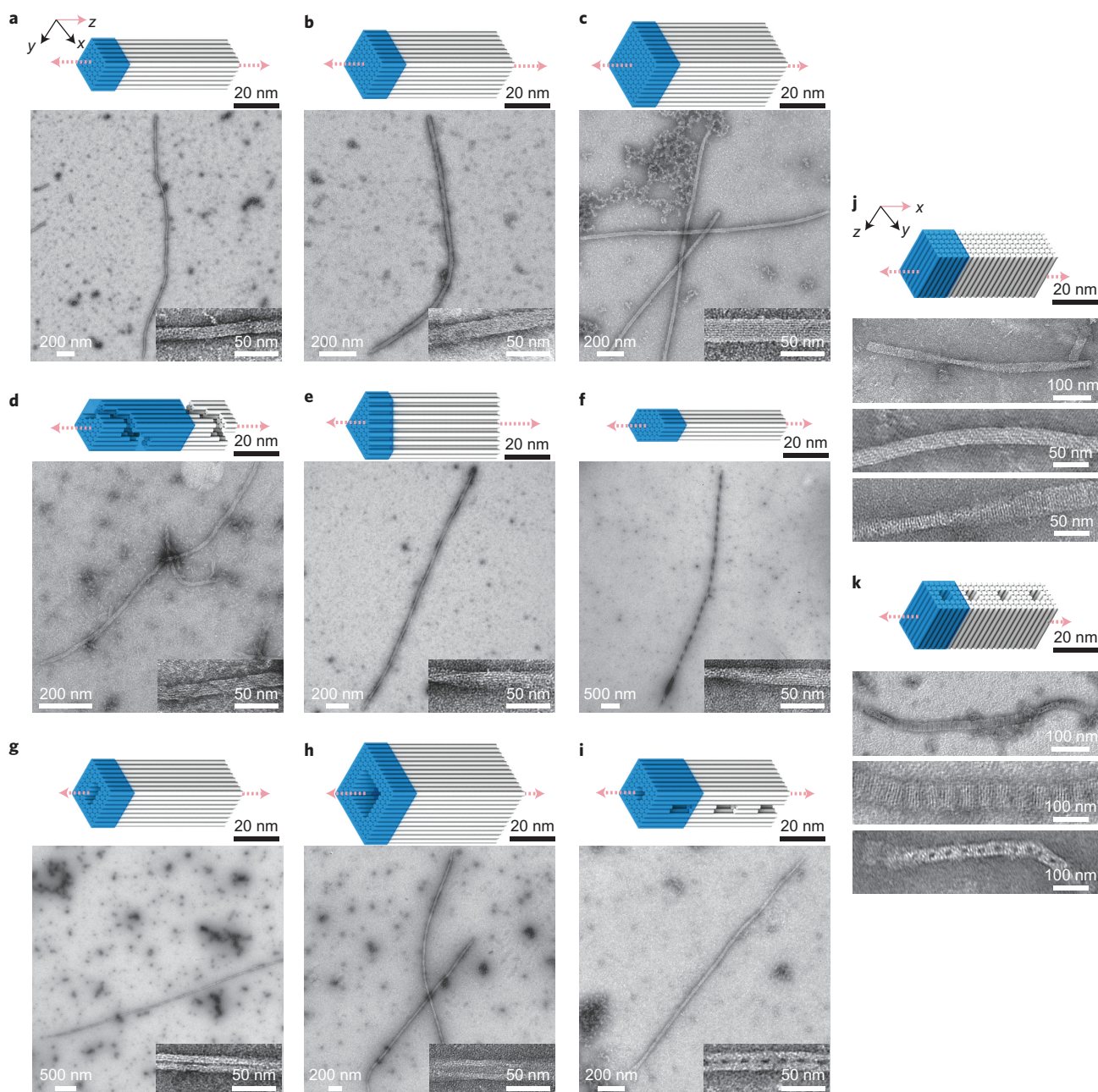
One-dimensional DNA-bundle crystals (Z-crystals)

Both solid Z-crystals (Fig. 2a–f) and Z-crystals with tunnels (Fig. 2g–i) were constructed successfully.

Solid Z-crystals with different cross-sectional shapes. We first constructed three solid Z-crystals with distinct square-shaped cross-sections (6H × 6H × 32B, 8H × 8H × 32B and 10H × 10H × 32B; Fig. 2a–c). We then demonstrated crystals with more complex cross-sections: a Z-8H × 8H × 128B-spiral crystal with a surface helical channel along the z axis (Fig. 2d), a Z-43H × 32B-triangle crystal (Fig. 2e) and a Z-44H × 32B-hexagon crystal (Fig. 2f). The spiral channel was clearly visible in the TEM image of the Z-8H × 8H × 128B-spiral crystal. However, many broken structures were also observed for this spiral crystal (Supplementary Fig. 6).

Z-crystals with tunnels. Three Z-crystals with tunnels were tested (Fig. 2g–i). The cross-section of the Z-56H × 32B-tunnel is an 8H × 8H square with a 2H × 4H rectangle removed from the centre (Fig. 2g). The Z-108H × 32B-tunnel has a 12H × 12H square cross-section with a 6H × 6H hole (Fig. 2h). The Z-60H × 64B-tunnel crystal contains a 2H × 2H tunnel along the z axis and 8H × 2H × 24B pores that intersect the 2H × 2H tunnel every 64 bp along the z axis (Fig. 2i). TEM images of the Z-60H × 64B-tunnel showed many splintered structures containing only half of the designed DNA helices, probably reflecting the weakening effect of the periodic 8H × 2H × 24B pores on the connections between the top and bottom halves of the structures along the y axis.

Figure 2 | One-dimensional DNA crystals. a–i, Z-crystals: cylinder models and TEM images. **a–c**, Z-crystals with solid cross-sections: 6H × 6H (**a**), 8H × 8H (**b**), 10H × 10H (**c**). **d–f**, Z-crystals with different cross-sectional shapes: 8H × 8H Z-crystal with right-handed spiral channel (**d**); 43H Z-crystal with triangle-shaped cross-section (**e**); 44H Z-crystal with hexagon-shaped cross-section (**f**). **g–i**, Z-crystals with porous cross-sections: 8H × 8H Z-crystal with a 2H × 4H tunnel (**g**); 12H × 12H Z-crystal with a 6H × 6H tunnel (**h**); 8H × 8H Z-crystal with a 2H × 2H tunnel and perpendicular 8H × 2H × 24B pores (**i**). **j,k**, Cylinder models (top) and TEM images (bottom) of X-crystals: X-6H × 6H × 64B-cuboid crystal (**j**); 6H × 6H X-crystal with 2H × 2H pores (**k**). Unit cells of crystals are denoted by blue boxes. See Supplementary Figs 3–12 for more TEM images.

All Z-crystals displayed a global right-handed twist, which probably resulted from the stress generated by the underwound design[17,42]. Zoomed-out TEM images of Z-crystals are provided in Supplementary Figs 3–11.
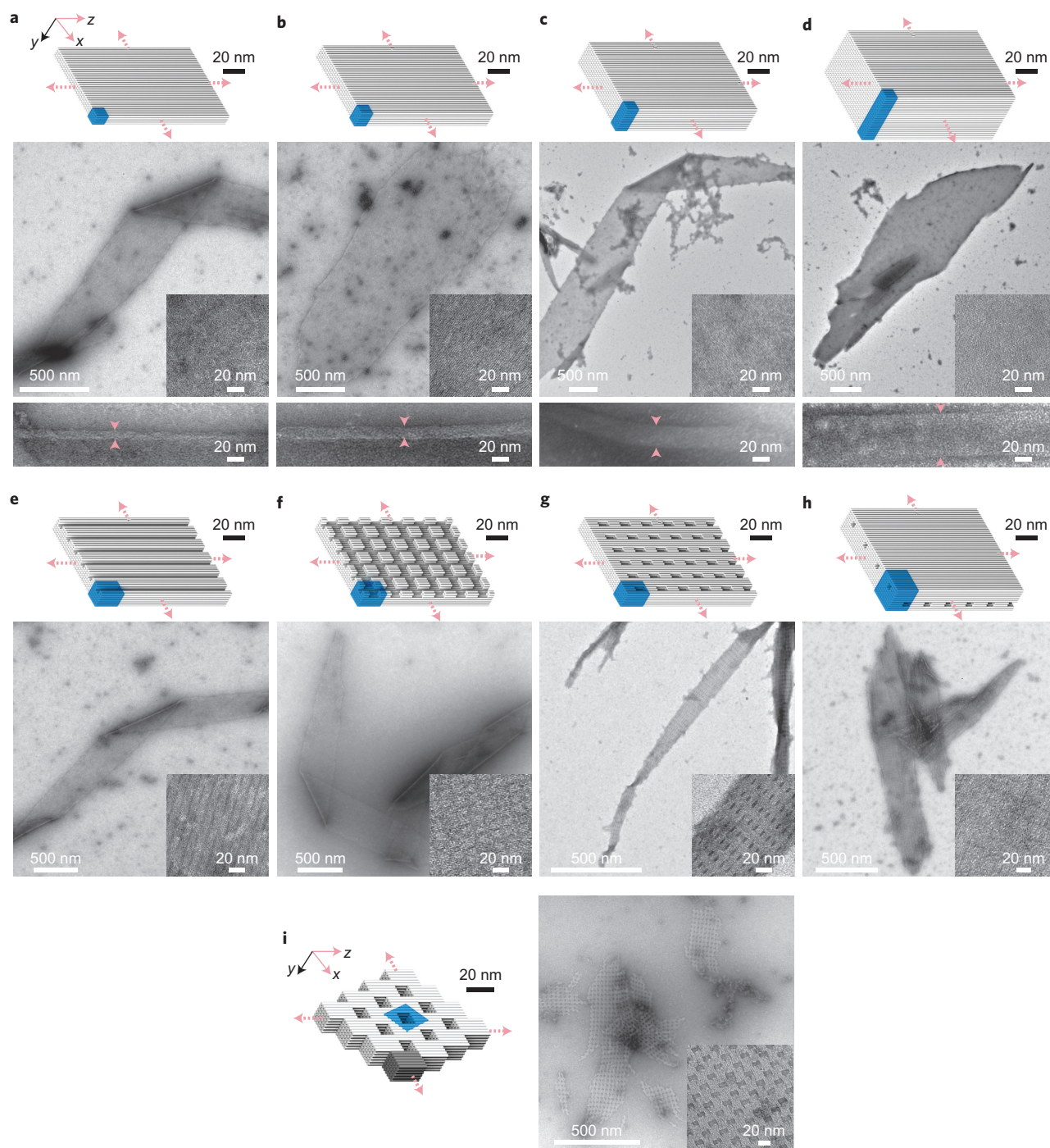
One-dimensional X-crystals

We constructed two one-dimensional crystals that extended along the x axis: an X-6H × 6H × 64B-cuboid crystal (Fig. 2j) and an X-32H × 64B-pore crystal (Fig. 2k). Both appeared well-formed and were observed to have grown up to a few hundred nanometres in length in TEM images. See Supplementary Fig. 12 for larger images.

Two-dimensional DNA multilayer crystals (ZX-crystals)

Solid ZX-crystals (Fig. 3a–d), ZX-crystals with channels, pores and tunnels (Fig. 3e–h) and an offset ZX-crystal (Fig. 3i) were successfully constructed.

Solid ZX-crystals. Four solid ZX-crystals were designed from 4H × 32B units that contained 4, 6, 10 and 20 layers of helices, respectively (Fig. 3a–d). The thickness of each ZX-crystal was directly measured at the crease where the crystal folded over onto itself in TEM images. The thicknesses of the 4-, 6-, 10- and 20-layer ZX-crystals were measured to be ~10, 15, 25 and 50 nm, respectively, proving all layers of the crystals were completely

Figure 3 | Two-dimensional multilayer ZX-crystals. Cylinder models (top) and TEM images (bottom) for each crystal. **a–d**, Solid ZX-crystals: 4-layer (**a**), 6-layer (**b**), 10-layer (**c**), 20-layer (**d**) solid ZX-crystals. Arrows indicate positions for thickness measurements of the crystals. **e–h**, ZX-crystals with channels, pores and tunnels: 6-layer crystal with 2H × 2H parallel channels (**e**); 6-layer crystal with two groups of crossing channels (2H × 2H channels that run parallel to the DNA helical axis and 2H × 32B channels that run perpendicular to the DNA helical axis) (**f**); 6-layer crystal with 2H × 6H × 32B pores (**g**); 10-layer crystal with two groups of non-contacting tunnels (2H × 2H tunnels parallel to the DNA helical axis and 2H × 24B tunnels perpendicular to DNA helical axis) (**h**). In **h**, the two groups of tunnels are separated by two layers of DNA helices. **i**, Offset-ZX-6H × 6H × 64B-cuboid ZX-crystal. The dark grey part represents a 6H × 6H × 64B-cuboid repeating unit. Unit cells of crystals are denoted by blue boxes. See Supplementary Figs 13–21 for more TEM images.

formed and that the width of each DNA helix was ~2.5 nm in diameter.

ZX-crystals with channels, pores and tunnels. We first designed three ZX-crystals from a 6H × 6H × 32B cuboid unit (Fig. 3e–g). Four helices were removed from the cuboid to generate ZX-32H × 64B-channel (Fig. 3e). The second design, ZX-32H ×

64B-cross-channel, was obtained by further removing a perpendicular 2H × 32B channel from ZX-32H × 64B-channel (Fig. 3f). The third design, ZX-6H × 6H × 64B-pore, contained a 2H × 4H × 32B vertical pore along the y axis in each cuboid unit (Fig. 3g). This design yielded narrow and long crystals. The most complex ZX-crystal design is the ZX-96H × 64B-cross-tunnel crystal (Fig. 3h). Its repeating unit can be considered as a

10H × 10H × 64B-cuboid with a 2H × 2H × 64B-pore along the z axis and with a 10H × 2H × 24B-pore along the x axis. In this structure, the design contains two types of parallel tunnel separated by two layers of DNA. These tunnels appear perpendicular when viewed from the ZX projection.

Offset two-dimensional ZX-crystal. We constructed a ZX-crystal that extended 6H × 6H × 64B-cuboid repeating units along the z axis and x axis using an 'offset-register' scheme: the crystal's z axis extension was shifted 4H along the x axis, and the crystal's x axis extension was shifted 32B along the z axis (Fig. 3i).

All ZX-crystals showed a small amount of right-handed twist, which also probably arose from the 10.67 bp/turn underwound design. As a result, we observed that the crystals sometimes appeared twisted and folded on top of themselves in TEM images. We also observed that all ZX-crystals grew faster along the z axis than the x axis, consistent with observations from previous crystal growth studies[26]. See Supplementary Figs 13–21 for more TEM images.

Two-dimensional DNA forest crystals (XY-crystals)

We constructed solid XY-crystals (Fig. 4a–d), XY-crystals with pores and surface channels (Fig. 4e–i) and XY-crystals that form a tube structure (Fig. 4j).

Solid XY-crystals. Solid XY-crystals of variable depths were constructed (Fig. 4a–d). Using a 4H × 4H-cuboid unit of various heights, we constructed four XY-crystals with 64B (21 nm), 128B (42 nm), 192B (63 nm) and 256B (84 nm) designed depths.

XY-crystals with pores and channels. XY-32H × 64B-pore and XY-32H × 128B-pore crystals were constructed (Fig. 4e,f). Both designs contained periodic 2H × 2H pores separated by 4H in each dimension. The two crystals resemble 21 nm and 42 nm porous membranes, respectively. Cryo-EM imaging was applied to these two crystals (Supplementary Fig. 22). Based on three-dimensional reconstruction data, their depths were measured to be 26 ± 2 nm (32H × 64B-pore) and 45 ± 3 nm (32H × 128B-pore), respectively (Fig. 4g,h), in good agreement with the theoretical values (21 nm and 42 nm). The slight discrepancy is likely to be a result of theoretical estimations not accounting for the single-stranded poly-T at the ends of the duplex. The depths of these two crystals were also measured by AFM to be ~16 nm and 36 nm, respectively (Supplementary Fig. 23). The smaller depths obtained from AFM probably reflect compression of the crystal by the cantilever.

An XY-4H × 8H × 96B-channel crystal was constructed (Fig. 4i). It contained a solid 64B (42 nm) base and parallel channels. The channels were 4H (10 nm) in width and 32B (21 nm) in height and were separated by four layers of helices.

A tube-shaped XY-crystal. An XY-4H × 4H × 32B-tube crystal (Fig. 4j) was designed using the same strategy as for the other XY-crystals. However, when assembled in 40 mM MgCl₂, this thin 32B (10.6 nm) XY-crystal formed a tube (Supplementary Figs 24 and 25) instead of a flat two-dimensional crystal, probably due to the uneven distribution of connections between helices (Supplementary Fig. 24).

Annealing the XY-4H × 4H × 32B-tube at higher MgCl₂ concentration produced tubes with larger diameters, presumably due to a greater reduction in repulsion between negatively charged DNA helices. At 60 mM MgCl₂ we observed many tubes with diameters between 140 and 300 nm (Supplementary Fig. 26). To further test our hypothesis that the tube formation is caused by the asymmetric distribution of crossovers, we designed an XY-4H × 4H × 32B-cuboid crystal in which the DNA bricks were arranged in an alternating fashion between layers[22]. Connections between helices in this

design were symmetrically distributed along both the x axis and the y axis (Supplementary Fig. 65). This alternating design produced only flat crystal structures (Supplementary Fig. 27). Additionally, the thicker 64, 128, 192 and 256B XY-crystals with non-alternating designs had 2, 4, 6 and 8 connections between each pair of neighbouring helices, respectively. No visible curvature was observed for these designs in TEM images (Supplementary Figs 28–31).

General observations. Unlike the ZX-crystals, the XY-crystals did not show a global right-handed twist. The lack of global twist can be explained by the following analysis. For simplicity, assume an XY-crystal forms a perfect cylinder containing n helices. The overall twist (in radians) of the cylinder is $\theta = TL/JG$, where T is the applied torque resulting from the underwound design, L is the helix length, G is the modulus rigidity of a helix, and J is the torsion constant. The first three parameters can be considered as constants. The torsion constant J for a cylinder as a function of cross-sectional (x–y plane) radius can be approximated as $\pi r^4/2$ (r^4 is proportional to n^2), where r is the circular cross-sectional radius. Thus, θ is inversely proportional to n^2. As an XY-crystal grows to include a large number of helices, its global twist θ rapidly becomes negligible.

As both growth directions (x axis and y axis) for an XY-crystal are perpendicular to the DNA helical axis, the XY-crystal grew in an isotropic fashion and did not exhibit any apparent directional preference. Because crystal growth along the x axis or y axis is slower than growth along the z axis (as discussed for ZX-crystals), the 72 h annealing often produces either no XY-crystals or XY-crystals smaller than 100 nm in their lateral dimensions. Accordingly, we used a 168 h annealing ramp for all XY-crystals.

XY-crystals provide a particularly attractive platform for DNA-directed guest molecule assembly. The surface of an XY-crystal can be considered as a 'breadboard'[13] on which guest molecules can be conveniently attached to the ends of DNA helices at 2.5 nm resolution in the lateral plane.

See Supplementary Figs 25–34 for more TEM images of XY-crystals.

Crystal growth mechanism

The non-hierarchical growth mechanism of DNA brick crystals was verified by the following experiments: (1) analysis of the boundaries of DNA brick crystals based on high-resolution TEM images revealed that these crystals lack well-defined, complete structural repeating units on their boundaries; (2) the annealing profile of the formation of the crystals revealed a single transition temperature (rather than two or more transition temperatures characteristic of hierarchically formed DNA crystals[32,36]); (3) time-lapse analysis of the TEM images and gel electrophoresis of the assembly process revealed the absence of repeating units of designed size.

Boundary analysis. We studied the edge of the XY-32H × 64B-pore crystal by counting the number of units that match that of the designed repeating unit (Supplementary Fig. 35). In hierarchically assembled crystals, the designed repeating units are first formed before they are assembled into a crystal. As a result, the edges of the crystal often consist of the shape of the designed repeating unit (for example, >90% of the edges of a previously reported hierarchically assembled crystal[36]; Supplementary Fig. 36). In contrast, only 2% of the edges of the XY-32H × 64B-pore brick crystal match that of the designed shape (Supplementary Fig. 37), consistent with a non-hierarchical assembly mechanism. See Supplementary Section 6.1 for more details.

Annealing curve. To study the annealing profile of the brick crystals we assembled the ZX-4H × 20H × 32B and XY-32H × 64B-pore crystals in the presence of SYBR Green I (Supplementary Figs 38 and 39).
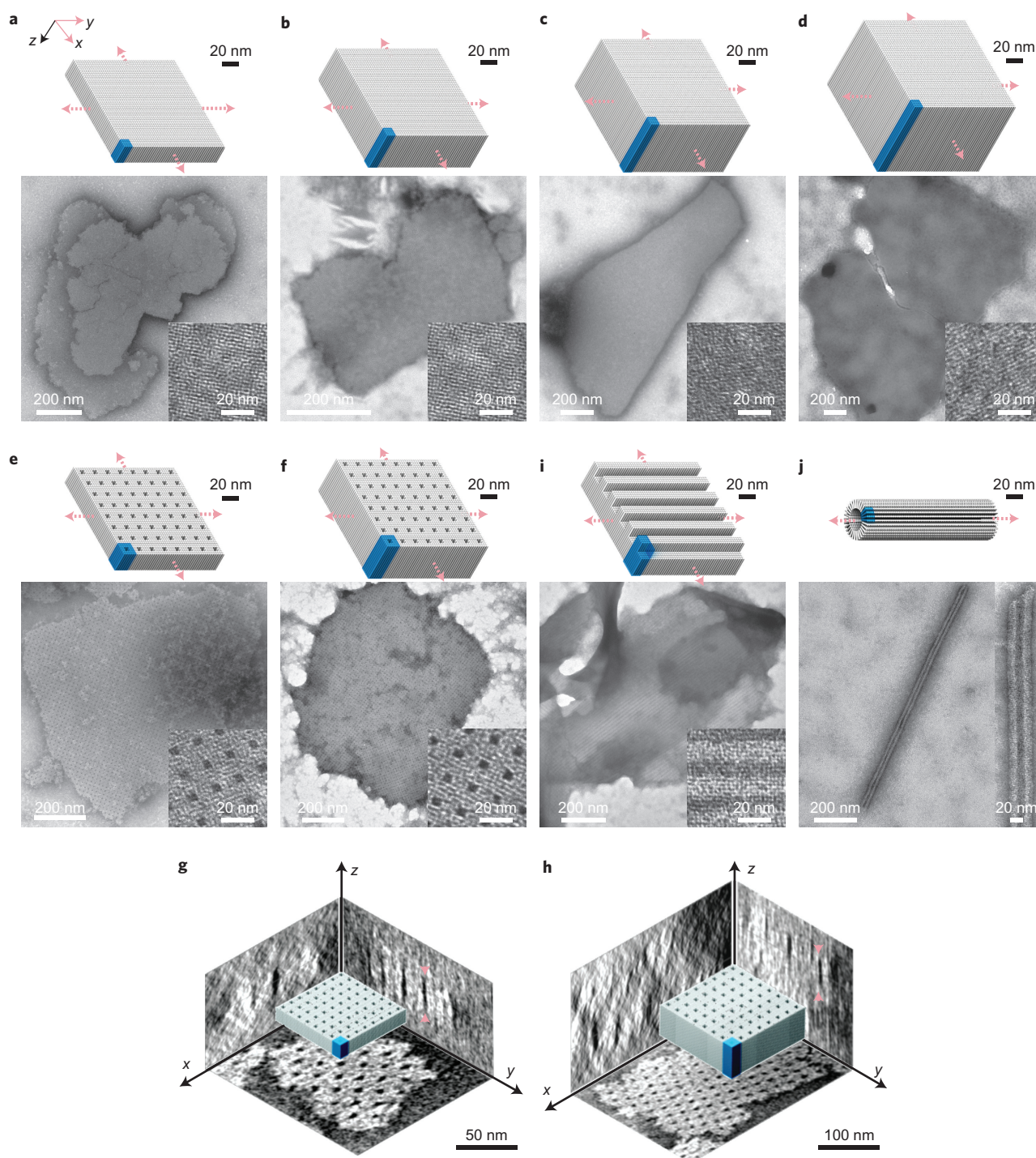
Figure 4 | Two-dimensional DNA forest XY-crystals. Cylinder models (top) and TEM images (bottom) for each crystal. **a–d**, Solid XY-crystals: 64B (**a**), 128B (**b**), 192B (**c**), 256B (**d**) solid XY-crystals designed from a 4H × 4H cuboid. **e,f**, XY-crystals with pores: 32 × 64B-pore XY-crystal with 2H × 2H × 64B parallel pores (**e**); 32H × 128B-pore XY-crystal with 2H × 2H × 128B parallel pores (**f**). **g,h**, Cryo-EM three-dimensional reconstruction images showing the three projections of the XY-32H × 64B-pore crystal (**g**) and the XY-32H × 128B-pore crystal (**h**). Arrows indicate positions of thickness measurements. **i**, A 96B XY-crystal with 4H × 32B parallel channels. **j**, A tube crystal formed by 32B helices with helical axis perpendicular to the tube axis. Unit cells of crystals are denoted by blue boxes. See Supplementary Figs 25–34 for more TEM images.

Annealing curves for both brick crystals depict a single, sharp transition peak, which occurred at ~40 °C for the ZX-crystal (Supplementary Fig. 38b,c) and 30 °C for the XY-crystal (Supplementary Fig. 39b,c), consistent with a non-hierarchical assembly process where individual component strands are directly incorporated into the lattices. See Supplementary Section 6.2 for more details.

Time-lapse analysis with gel electrophoresis and TEM. Time points before, at and after the transition temperature were sampled for both the above two ZX- and XY-crystals to confirm the lack of well-formed, discrete repeating units. Gel electrophoresis showed no intermediate band between the well and monomers (Supplementary Figs 38d and 39d), as expected. Although TEM imaging revealed some small, randomly sized and
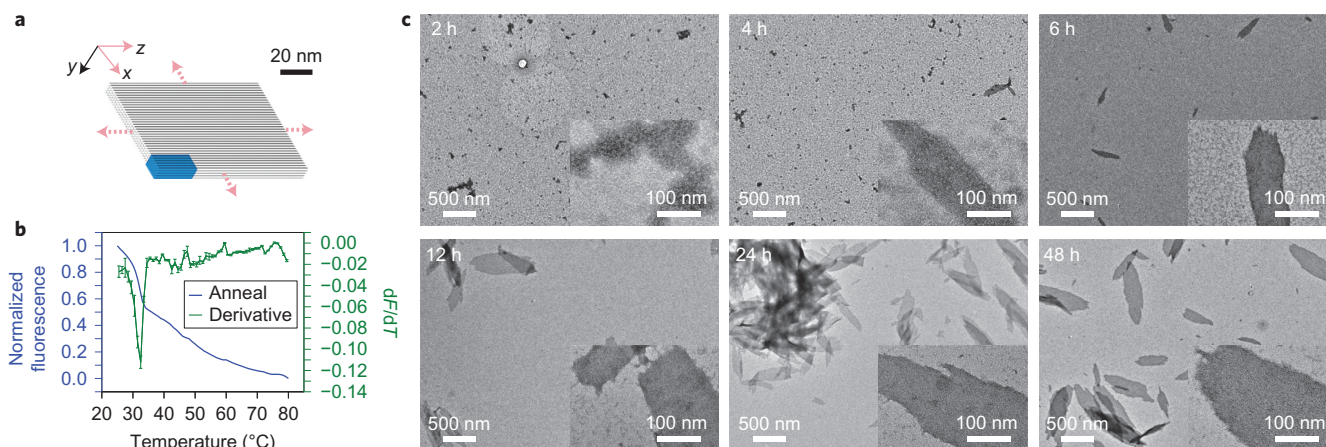
Figure 5 | Isothermal assembly of brick crystals. a, Cylinder model of a ZX-6H × 4H × 96B crystal. **b**, Annealing curve (blue) with the derivative of the fluorescence with respect to temperature (green) of the ZX-6H × 4H × 96B crystal. Annealing curves were obtained in the presence of 0.3 × SYBR Green I at 500 nM of each strand. Error bars represent standard error from the mean acquired from three measurements. **c**, TEM images of the ZX-6H × 4H × 96B crystal incubated at 33 °C for various durations. Samples were diluted four times before deposition on the TEM grids.

shaped clusters of strands, no uniformly sized and shape-defined structures were observed, supporting the designed non-hierarchical assembly mechanism (Supplementary Figs 38e and 39e). See Supplementary Section 6.2 for more details.

Isothermal assembly

The single transition temperature of the DNA brick crystallization suggests that these crystals should be able to assemble isothermally. We therefore assembled a ZX-6H × 4H × 96B-cuboid crystal iso-thermally at the observed annealing transition temperature of 33 °C (Fig. 5a, Supplementary Fig. 40c). Gel electrophoresis showed no discrete monomer band during annealing (Supplementary Fig. 40d). Time-lapse TEM images further supported the non-hierarchical assembly mechanism: structures around 100 nm in size appeared after 2 h and rapidly grew to micrometre-sized structures by 48 h (Fig. 5c). See Supplementary Section 6.3 for more details.

Yield and defect analysis

We used crystal deposition density and the strand depletion ratio to estimate the approximate yield of brick crystals. After four-times dilution, an isothermally assembled ZX-6H × 4H × 96B sample produced 0.23 structures per μm^2 on a TEM grid (Supplementary Fig. 41), while Förster resonance energy transfer analysis of dye-labelled ZX-6H × 6H × 64B sample suggested an 80% strand depletion ratio (Supplementary Fig. 42). Analysis of the pore morphology of XY-32H × 64B-pore TEM images indicated a 9%

defect rate (Supplementary Fig. 43). See Supplementary Section 7 for more details.

Patterning gold nanoparticles

Gold nanoparticles have previously been arranged into discrete patterns[39,40,43] and single-layer periodic patterns[35] using DNA structures as templates. However, it remains challenging to form close-packed periodic patterns, especially multilayer patterns, of gold nanoparticles. This challenge is addressed here using DNA crystals. We constructed two close-packed gold-nanoparticle super-structures on DNA brick crystals: (1) parallel lines of gold particles arranged on a ZX-4H × 6H × 96B-channel crystal (Supplementary Fig. 44) spaced on average 2 nm apart (Fig. 6a,b), and (2) parallel gold-nanoparticle monolayers, with each particle spaced on average 1–2 nm apart, on an XY-4H × 4H × 64-cuboid (Fig. 6c–e). Aligning gold nanoparticles into micrometre-scale ordered arrays is required in diverse plasmonic applications. In particular, nano-particle arrays with sub-2 nm face-to-face spacing are expected to exhibit strong plasmonic coupling[44]. See Supplementary Section 8 for more experimental details.

Discussion

Crystallization of increasingly large macromolecular complexes can be challenging. Traditionally, the process is hierarchical; that is, the complexes incorporate into the crystal as preformed monomeric units[26–32,34–38]. However, the homogeneity of complex monomers
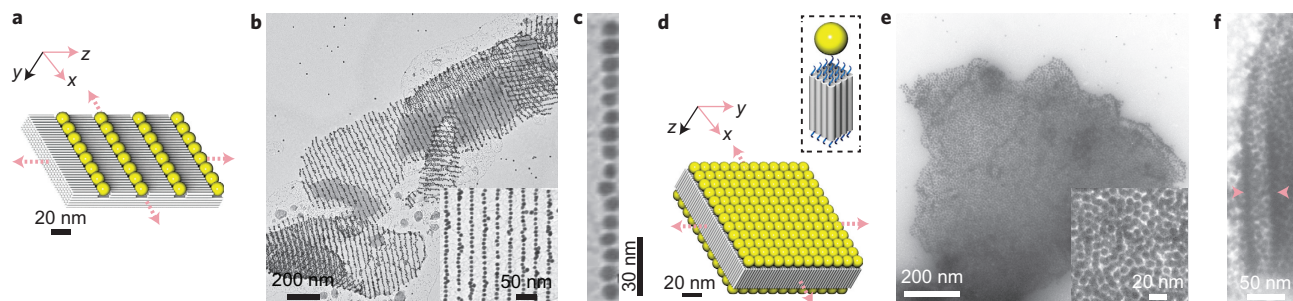
Figure 6 | Gold nanoparticles patterned using DNA brick crystals. a–c, Model (**a**) and TEM images (**b,c**) of parallel lines of 10 nm gold nanoparticles closely packed on a ZX-4H × 6H × 96-channel crystal. **c**, Zoomed-in TEM image of a single chain of gold nanoparticles. **d–f**, Model (**d**) and TEM images (**e,f**) of close-packed gold-nanoparticle monolayers formed on the top and bottom surfaces of an XY-4H × 4H × 64B-cuboid crystal. Inset of **d**: single-stranded poly-T extensions on each end of the helix and a 10 nm gold nanoparticle occupying a 4H × 4H surface. A crystal displays curvatures on the edge (**f**). Pink arrows indicate the curved positions where the two gold-nanoparticle monolayers can be seen.

is often difficult to ensure and the addition of a defective monomer can compromise the growth of a well-ordered crystal. Furthermore, the kinetics of joining large monomers can be slow because of their size, especially in the case when they repel each other due to like charges. Finally, effective crystallization is thought to require error correction that involves near-equilibrium incorporation and dissociation of monomers to erase defects on the path to the lowest energy state. Therefore, if the strength of the interaction between monomers is too strong, which is more likely for large structures, irreversible rather than reversible self-assembly may dominate, resulting in defective crystals.

In contrast, our DNA brick framework explores a non-hierarchical route to crystallization that achieves reversible assembly of rapidly diffusing subcomponents without sacrificing the complexity of the larger repeating unit in the final crystals. Using a modular strategy that utilizes standardized components—such as our DNA bricks—a repeating unit can contain thousands of base pairs, enabling the implementation of designs bearing intricate features. Although we define a repeating unit for ease of design, there is no difference between bricks within each repeating unit and those that connect the repeating units, so bricks can be added to or subtracted from the growing crystal one at a time. A corollary is that the boundary where one repeating unit begins and the next one ends is arbitrary.

Microscale two-dimensional DNA brick crystals with prescribed depths and three-dimensional nanoscale features provide a new platform for developing diverse applications. In biophysics, host–guest two-dimensional DNA crystals could facilitate cryo-EM imaging and three-dimensional reconstruction of protein structures[45]. Thicker two-dimensional crystals are more rigid and resistant to dynamic thermal fluctuations, providing better translational alignment of proteins; their three-dimensional cavities could potentially hold the guest molecule in a specific conformation, providing better orientational alignment within each unit cell. In photovoltaics, bottom-up self-assembly of nanomaterials, such as nanowires[46], provides a promising route to producing high-efficiency photovoltaic devices. DNA brick crystals may prove useful for self-assembling three-dimensional nanomaterials with nanometre precision, thus achieving enhanced cooperation effects and energy conversion efficiency for photovoltaic devices. In nanofabrication, these two-dimensional DNA crystals may serve as etching masks for fabricating diverse inorganic-materials-based devices and circuits, providing better shape programmability than current block-copolymer-based masks[5].

Methods

Design diagrams. DNA strand diagrams are provided in Supplementary Section 9 (Supplementary Figs 45–76).

Sample preparation. DNA strands were synthesized by Integrated DNA Technology (www.idtdna.com). To assemble the structures, unpurified DNA strands were mixed in an equimolar stoichiometric ratio from a 100 μM stock in 0.5 × Tris/EDTA buffer (5 mM Tris, pH 7.9, 1 mM EDTA) supplemented with 40 mM $MgCl_2$. For Z-crystals and ZX-crystals, the final concentration of each strand was adjusted to roughly 200 nM. For X-crystals and XY-crystals, the highest possible concentration (no addition of extra water) was used for annealing.

Annealing ramps and isothermal assembly. The strand mixture was annealed in a PCR thermo cycler using a fast linear cooling step from 80 °C to 60 °C over 1 h, then a 72 h or 168 h linear cooling ramp from 60 °C to 25 °C. The annealing ramps were named according to the length of the second cooling step (as 72 h annealing or 168 h annealing). Most ZX-crystals were folded using 72 h annealing, except the ZX-96H × 64B-cross-tunnels, which used 168 h annealing. All XY-crystals were folded with 168 h annealing. For isothermal assembly of DNA crystals, the sample solution was incubated at 33 °C for up to 48 h.

DNA modification of 10 nm gold nanoparticles. Conjugation of thiolated DNA onto 10 nm gold nanoparticles was achieved following a previously reported protocol[47]. In a typical experiment, 20 μl 2.5 μM phosphine-coated 10 nm gold nanoparticles were mixed with 0.5 μl 2 M $NaNO_3$ and 0.65 μl 100 μM thiolated DNA in 0.25 × Tris/borate/EDTA (TBE) buffer. The reaction solution was incubated

at room temperature for 36 h in the dark. After that, the reaction solution was loaded into 1% agarose gel containing 0.5 × TBE buffer. The electrophoresis was running at 95 V for 1 h in a gel box on an ice-water bath. The purple band was recovered by pestle crushing, followed by centrifugation for 3 min at 10,000 r.p.m. at room temperature using 'Freeze' N Squeeze' DNA Gel Extraction spin columns (Bio-Rad). Recovered DNA-modified gold nanoparticles were stored at 4 °C in the dark for further use. The sequence for the thiolated DNA was 5′-AAAAAAAAAA-/3ThioMC3-D/.

Gold-nanoparticle decoration of DNA crystals. To 15 μl 400 mM NaCl solution, 0.8 μl (ZX-4H × 6H × 96B-channel crystal) or 0.6 μl (XY-4H × 4H × 64B-cuboid crystal) DNA samples were added. Then, 0.2 μl 95 nM 10 nm gold nanoparticles were introduced. After pipetting 50 times, the reaction mixture was left at room temperature for 3 h in the dark.

TEM imaging. For imaging, 2.5 μl annealed sample was adsorbed for 2 min onto glow-discharged, carbon-coated TEM grids. The grids were then stained for 10 s using a 2% aqueous uranyl formate solution containing 25 mM NaOH. Imaging was performed using a JEOL JEM-1400 TEM operating at 80 kV.

Cryo-EM imaging. A 5 μl droplet of the crystal sample was added onto the positively charged carbon grids, blotted for 5.5 s, and plunge-frozen in liquid ethane using a Vitrobot (FEI). Grids were then loaded into a Titan Krios TEM (FEI), which was operated at 300 kV with nominal −3 μm defocus using a dose of 1.5 e Å^{-2}. The specimen was tilted in <2° increments over a total angular range of ±60°. All images were obtained using automated data-acquisition software. Three-dimensional reconstructions from the above tilt series were carried out with the weighted back-projection method, and further analysis of tomograms was done using IMOD software[48].

Annealing and melting curves. Strands (500 nM) were folded (following the annealing ramp protocol described above) in the presence of 0.3 × SYBR Green I using the Eppendorf Mastercycler realplex 4 PCR. Samples were read once during the first cooling step and four times during the second cooling step. Following annealing, the same samples were melted at a rate of 0.2 °C min^{-1}. Samples (9 μl) were removed during annealing or melting for TEM and gel electrophoresis analysis.

Agarose gel electrophoresis. Annealed samples were subjected to 1.5% or 2% native agarose gel electrophoresis for 2 h (gel prepared in 0.5 × TBE buffer supplemented with 10 mM $MgCl_2$ and 0.005% (vol/vol) EtBr) or 1 × SYBR Safe in an ice-water bath.

AFM imaging. AFM images were obtained using a MultiMode VIII SPM (Bruker) equipped with a liquid cell. A 2 μl volume of sample was placed onto the surface of highly ordered pyrolytic graphite, which was pretreated with ultraviolet-ozone for 30 s. The 50 μl of Tris/acetate/EDTA buffer (12.5 mM Mg^{2+}, 5 mM Ni^+) was added into the liquid cell, and images were collected using silicon nitride cantilevers (Olympus).

References

1. Melosh, N. A. *et al.* Ultrahigh-density nanowire lattices and circuits. *Science* **300,** 112–115 (2003).
2. Qi, M. *et al.* A three-dimensional optical photonic crystal with designed point defects. *Nature* **429,** 538–542 (2004).
3. Liu, N., Hentschel, M., Weiss, T., Alivisatos, A. P. & Giessen, H. Three-dimensional plasmon rulers. *Science* **332,** 1407–1410 (2011).
4. Tang, C. B., Lennon, E. M., Fredrickson, G. H., Kramer, E. J. & Hawker, C. J. Evolution of block copolymer lithography to highly ordered square arrays. *Science* **322,** 429–432 (2008).
5. Tavakkoli, K. G. A. *et al.* Templating three-dimensional self-assembled structures in bilayer block copolymer films. *Science* **336,** 1294–1298 (2012).
6. Liu, N. *et al.* Three-dimensional photonic metamaterials at optical frequencies. *Nature Mater.* **7,** 31–37 (2008).
7. Edward, E. W., Montague, M. F., Solak, H. H., Hawker, C. J. & Nealey, P. F. Precise control over molecular dimensions of block-copolymer domains using the interfacial energy of chemically nanopatterned substrates. *Adv. Mater.* **16,** 1315–1319 (2004).
8. Kim, S. O. *et al.* Novel complex nanostructure from directed assembly of block copolymers on incommensurate surface patterns. *Adv. Mater.* **19,** 3271–3275 (2007).
9. Seeman, N. C. Nucleic acid junctions and lattices. *J. Theor. Biol.* **99,** 237–247 (1982).
10. Chen, J. & Seeman, N. C. The synthesis from DNA of a molecule with the connectivity of a cube. *Nature* **350,** 631–633 (1991).
11. Fu, T. J. & Seeman, N. C. DNA double-crossover molecules. *Biochemistry* **32,** 3211–3220 (1993).
12. Shih, W. M., Quispe, J. D. & Joyce, G. F. A 1.7-kilobase single-stranded DNA that folds into a nanoscale octahedron. *Nature* **427,** 618–621 (2004).
13. Rothemund, P. W. K. Folding DNA to create nanoscale shapes and patterns. *Nature* **440,** 297–302 (2006).

14. He, Y. *et al.* Hierarchical self-assembly of DNA into symmetric supramolecular polyhedra. *Nature* **452,** 198–201 (2008).
15. Andersen, E. S. *et al.* Self-assembly of a nanoscale DNA box with a controllable lid. *Nature* **459,** 73–76 (2009).
16. Douglas, S. M. *et al.* Self-assembly of DNA into nanoscale three-dimensional shapes. *Nature* **459,** 414–418 (2009).
17. Dietz, H., Douglas, S. M. & Shih, W. M. Folding DNA into twisted and curved nanoscale shapes. *Science* **325,** 725–730 (2009).
18. Woo, S. & Rothemund, P. W. K. Programmable molecular recognition based on the geometry of DNA nanostructures. *Nature Chem.* **3,** 620–627 (2011).
19. Han, D. *et al.* DNA origami with complex curvatures in three-dimensional space. *Science* **332,** 342–346 (2011).
20. Sobczak, J-P. J., Martin, T. G., Gerling, T. & Dietz, H. Rapid folding of DNA into nanoscale shapes at constant temperature. *Science* **338,** 1458–1461 (2012).
21. Wei, B., Dai, M. & Yin, P. Complex shapes self-assembled from single-stranded DNA tiles. *Nature* **485,** 623–626 (2012).
22. Ke, Y., Ong, L. L., Shih, W. M. & Yin, P. Three-dimensional structures self-assembled from DNA bricks. *Science* **338,** 1177–1183 (2012).
23. Han, D. *et al.* DNA gridiron nanostructures based on four-arm junctions. *Science* **339,** 1412–1415 (2013).
24. Wei, B. *et al.* Design space for complex DNA structures. *J. Am. Chem. Soc.* **135,** 18080–18088 (2013).
25. Iinuma, R. *et al.* Polyhedra self-assembled from DNA tripods and characterized with 3D DNA-PAINT. *Science* **344,** 65–69 (2014).
26. Winfree, E., Liu, F., Wenzler, L. A. & Seeman, N. C. Design and self-assembly of two-dimensional DNA crystals. *Nature* **394,** 539–544 (1998).
27. Yan, H., Park, S. H., Finkelstein, G., Reif, J. H. & LaBean, T. H. DNA-templated self-assembly of protein arrays and highly conductive nanowires. *Science* **301,** 1882–1884 (2003).
28. Liu, D., Wang, M., Deng, Z., Walulu, R. & Mao, C. Tensegrity: construction of rigid DNA triangles with flexible four-arm DNA junctions. *J. Am. Chem. Soc.* **126,** 2324–2325 (2004).
29. Rothemund, P. W. K., Papadakis, N. & Winfree, E. Algorithmic self-assembly of DNA Sierpinski triangles. *PLoS Biol.* **2,** 2041–2053 (2004).
30. He, Y., Chen, Y., Liu, H., Ribbe, A. E. & Mao, C. Self-assembly of hexagonal DNA two-dimensional (2D) arrays. *J. Am. Chem. Soc.* **127,** 12202–12203 (2005).
31. Malo, J. *et al.* Engineering a 2D protein–DNA crystal. *Angew. Chem. Int. Ed.* **44,** 3057–3061 (2005).
32. Ke, Y., Liu, Y., Zhang, J. P. & Yan, H. A study of DNA tube formation mechanisms using 4-, 8-, and 12-helix DNA nanostructures. *J. Am. Chem. Soc.* **128,** 4414–4421 (2006).
33. Yin, P. *et al.* Programming DNA tube circumferences. *Science* **321,** 824–826 (2008).
34. Zheng, J. P. *et al.* From molecular to macroscopic via the rational design of a self-assembled 3D DNA crystal. *Nature* **461,** 74–77 (2009).
35. Sharma, J. *et al.* Control of self-assembly of DNA tubules through integration of gold nanoparticles. *Science* **323,** 112–116 (2009).
36. Liu, W., Zhong, H. & Seeman, N. C. Crystalline two dimensional DNA origami arrays. *Angew. Chem. Int. Ed.* **50,** 264–267 (2011).
37. Majumder, U., Rangnekar, A., Gothelf, K. V., Reif, J. H. & LaBean, T. H. Design and construction of double-decker tile as a route to three-dimensional periodic assembly of DNA. *J. Am. Chem. Soc.* **133,** 3843–3845 (2011).
38. Wang, T., Schiffels, D., Cuesta, S. M., Fygenson, D. K. & Seeman, N. C. Design and characterization of 1D nanotubes and 2D periodic arrays self-assembled from DNA multi-helix bundles. *J. Am. Chem. Soc.* **134,** 1606–1616 (2012).
39. Kuzyk, A. *et al.* DNA-based self-assembly of chiral plasmonic nanostructures with tailored optical response. *Nature* **483,** 311–314 (2012).
40. Acuna, G. P. *et al.* Fluorescence enhancement at docking sites of DNA-directed self-assembled nanoantennas. *Science* **338,** 506–510 (2012).
41. Park, S. *et al.* Macroscopic 10-terabit per square-inch arrays from block copolymers with lateral order. *Science* **323,** 1030–1033 (2009).
42. Ke, Y. *et al.* Multilayer DNA origami packed on a square lattice. *J. Am. Chem. Soc.* **131,** 15903–15908 (2009).
43. Aldaye, F. A. & Sleiman, H. F. Sequential self-assembly of a DNA hexagon as a template for the organization of gold nanoparticles. *Angew. Chem. Int. Ed.* **45,** 2204–2209 (2006).
44. Tan, S. F. *et al.* Quantum plasmon resonances controlled by molecular tunnel junctions. *Science* **343,** 1496–1499 (2014).
45. Selmi, D. N. *et al.* DNA-templated protein arrays for single-molecule imaging. *Nano Lett.* **11,** 657–660 (2011).
46. Dang, X. N. *et al.* Virus-templated self-assembled single-walled carbon nanotubes for highly efficient electron collection in photovoltaic devices. *Nature Nanotech.* **6,** 377–384 (2011).
47. Sharma, J. *et al.* Toward reliable gold nanoparticle patterning on self-assembled DNA nanoscaffold. *J. Am. Chem. Soc.* **130,** 7820–7821 (2008).
48. Kremer, J. R., Mastronarde, D. N. & McIntosh, J. R. Computer visualization of three dimensional image data using IMOD. *J. Struct. Biol.* **116,** 71–76 (1996).

Acknowledgements

Author contributions

Y.K., L.L.O. and W.S. made equal contributions to this work. Y.K. conceived the project, designed and performed the experiments, analysed the data and wrote the paper. L.L.O. and W.S. designed and performed the experiments, analysed the data and wrote the paper. J.S. and M.D. performed the cryo-EM and AFM experiments, analysed the data and wrote the paper. W.M.S discussed the results and wrote the paper. P.Y. conceived, designed and supervised the study, interpreted the data and wrote the paper.

Additional information

Supplementary information is available in the online version of the paper. Reprints and permissions information is available online at www.nature.com/reprints. Correspondence and requests for materials should be addressed to P.Y. and Y.K.

Competing financial interests

A provisional US patent application based on the work described in this manuscript has been filed.